Bioprinting 23 (2021) e00144

Contents lists available at ScienceDirect

Bioprinting

journal homepage: www.sciencedirect.com/journal/bioprinting

# Real-time imaging and analysis of cell-hydrogel interplay within an extrusion-bioprinting capillary

Gowsihan Poologasundarampillai [a,*], Abdelrahman Haweet [a,b,1], Soher Nagi Jayash [a], George Morgan [c], James E. Moore Jr. [c], Alessia Candeo [b,d,**]

[a] School of Dentistry, Institute of Clinical Sciences, University of Birmingham, Birmingham, B5 7EG, UK
[b] Central Laser Facility—Science & Technology Facility Council, The Research Complex at Harwell, Rutherford Appleton Laboratory, Harwell Campus, Didcot, Oxfordshire, OX11 0FA, UK
[c] Department of Bioengineering, Imperial College London, South Kensington, SW7 2AZ, UK
[d] Dipartimento di Fisica, Politecnico di Milano, Piazza Leonardo da Vinci 32, 20133 Milano, Italy

ARTICLE INFO

*Keywords:*
3D bioprinting
Bioinks
Light-sheet fluorescence microscopy
Capillary flow imaging
Multiphase flow

ABSTRACT

Additive manufacturing platforms are transforming research and industrial sectors worldwide. In regenerative medicine and pharmaceutical applications, they facilitate the development of patient-specific devices for implantation, as well as in vitro models of tissues and organs for disease modelling and drug screening. A key example is extrusion-based bioprinting, where a bioink that contains cells, biomolecules and a support matrix (often hydrogel), is extruded through a narrow capillary onto a platform forming the desired structure. The printing parameters and hydrogel flow behavior likely determine the extent to which cells are damaged mechanically as they pass through the capillary. Here, we present direct observations of the hydrogels and suspended cells during the printing process to help elucidate conditions potentially leading to mechanical damage and cell death. Light-sheet fluorescence microscopy was applied to observe the real-time flow of bioinks through a capillary mimicking the conditions found in bioprinting. Bioink formulations exhibiting constant and shear thinning viscosities, along with UV-crosslinked gelatin methacrylol (GelMA) were studied, and cell viability of post-printed gels were measured via fluorescent imaging. Cell tracking enabled flow profiles of bioinks to be deduced. In agreement with current flow simulations, the constant and shear thinning formulations displayed a Poiseuille flow profile although with a plug velocity profile for the latter. The UV-crosslinked GelMA formulation exhibited a two-phase annular flow with gel morphologies depicting gross-melt fractures attributed to over-gelled hydrogels. Cell viability was higher in UV-crosslinked GelMA at high flow rates compared to uncrosslinked GelMA. The findings presented here will improve modeling cell-material flow during bioprinting through accurate estimation of flow conditions, in particular for complex materials. The novel imaging approach could be further exploited to provide process monitoring and feedback to improve the outcomes of 3D bioprinting.

## 1. Introduction

Bioprinting allows automated structuring of living materials (cells, spheroids and organoids) into complex, predefined architectures in a layer-by-layer fashion. The bioprinted structures can then be matured in vitro to generate tissue and organ-mimics with potential for use in drug discovery and regenerative medicine [1–3]. Extrusion-based 3D bioprinting has been adopted in the tissue engineering community due to its high speed of fabrication, precision and simplicity [4–8], driven by advances in modern robotics and bioink formulations [9–13]. Even though there are variations [4] to this technique, generally a living substance is delivered via a hydrogel through a thin capillary tube with diameters ranging from 50 μm to 1 mm [7].

Despite the many benefits associated with the extrusion technique, the mechanical environment experienced by the cells as they are extruded through the bioprinter capillary can be detrimental [14–16].

* Corresponding author.
** Corresponding author.
*E-mail addresses:* G.Poologasundarampillai@bham.ac.uk (G. Poologasundarampillai), abdelrahman.s.haweet@gmail.com (A. Haweet), soheernaji20@yahoo.com (S.N. Jayash), george.morgan16@imperial.ac.uk (G. Morgan), james.moore.jr@imperial.ac.uk (J.E. Moore), alessia.candeo@polimi.it (A. Candeo).
[1] Co-first author.

https://doi.org/10.1016/j.bprint.2021.e00144
Received 17 February 2021; Received in revised form 11 April 2021; Accepted 12 April 2021
Available online 12 May 2021

This may be exacerbated with the use of smaller diameter capillaries, large flow rates and high viscosity hydrogels necessary for rapid printing with adequate resolution and shape fidelity. These factors affect cell viability, phenotype and functionality [14,17–20]. There are reports of attempts to minimize cell damage by developing innovative hydrogels and optimizing printing parameters, supported by models of the flow of hydrogels through capillaries [15,17–22]. Aguado et al. [15] found that suspending cells in hydrogels helped reduce mechanical damage following injection and proposed that cell viability could be increased by minimizing extensional forces experienced by cells in the converging region upstream of the needle. They dismissed shear forces experienced in the needle as having negligible influence on cell viability based on separate experiments in a cone and plate viscometer. This study lacked direct observation of cell and fluid movements in the actual bioprinting pathway. Subsequently, several others [17,20,21,23] have predicted shear stresses experienced by the cells in a bioprinter capillary and found cell viability decreased with increasing shear stress. Lucas et al. [20] found that viability was well predicted with a combination of maximum wall shear stress, exposure time and bioink viscosity. Paxton et al. [24] presented an analysis of the extrusion velocity, shear stress and retention time through a capillary for materials with various viscosities including, shear thinning hydrogels with yield stress behavior which they suggested could help to reduce the percentage of cells experiencing damaging shear. Most hydrogels exhibit a 'shear thinning' behavior in which apparent viscosity decreases with increasing shear stress [25]. Pluronic® F127, used primarily as a fugitive ink in biofabrication, is a shear thinning fluid with a yield shear stress, above which Pluronic® behaves like a fluid [26]. Yield stress fluids also support printing with their ability to recover their solid behavior after shearing is removed. This improves accuracy and shape fidelity. Several biopolymer hydrogels including alginate, hyaluronic acid and functionalized gelatin (GelMA) are shear thinning [15,22,24,27–31]. However, printed constructs often display structural irregularities with inhomogeneous and fractured filaments [22]. This has been associated with over-gelled bioinks and/or an excessive degree of crosslinking [32]. Optimal bioink design [33] therefore involves a careful balance of properties that maximize cell survival and structural stability of the construct.

Three-dimensional continuous imaging during extrusion would enable novel insights on the dynamics of bioink flow and cell movement, complimenting ex situ rheological studies and mathematical models. Furthermore, it would enable investigation of complex capillary designs (cylindrical, rectangular, conical or serrated) and surface free energies and various cell types and densities to further the development of 3D bioprinting and printed constructs. In addition, for printed constructs to be successfully translated to clinical applications, process monitoring through continuous imaging will be critical for quality assurance and regulatory compliance [33].

Bright and dark field microscopy based particle image velocimetry (PIV) [34–37] and particle tracking velocimetry (PTV) [38] have been successfully employed in microfluidics, but are fundamentally two-dimensional techniques. The combination of confocal microscopy with PIV and PTV allows for 3D studies thanks to the rejection of background contribution from out of focus planes, superior spatial resolution and improved contrast [39,40], though the short working distances of typical objectives limit the use of the technique to channel dimensions of 50–100 μm. Tomographic PIV [41] and PTV [42], obtained with multi-camera, stereoscopic and holographic approaches, do allow the observation of larger volumes, but require tedious alignment, calibration protocols and postprocessing steps, which makes them impractical for continuous live imaging [43,44]. Furthermore, PIV and PTV work best with a dense ensemble of particles that typically exceeds cell concentrations used in bioprinting.

In this study, light sheet fluorescence microscopy (LSFM) was employed to quantify flow of cell-laden hydrogels through a capillary in real-time to provide quantitative information on cell-hydrogel interplay in a capillary tube that mimics the portion of the extrusion bioprinting process in which cells are most likely to be damaged. In LSFM, the illumination and detection optical pathways are decoupled and orthogonal, offering 'gentle' optical sectioning capability at high speed image acquisition minimizing the background noise and photodamage to the sample [45–51]. LSFM has been used to image flow within microfluidic devices and in flow cytometry [52–56] because of its outstanding spatio-temporal resolution and its higher signal-to-noise ratio (SNR) in comparison to standard microscopy techniques. Information obtained from applying LSFM to bioprinting can facilitate the optimization of 3D bioprinting; contribute to developing 'universal' bioink and printing setups and nozzle geometries.

## 2. Material and methods

All materials were purchased from Sigma Aldrich unless otherwise stated and used as received. GelMA, Pluronic® and agar hydrogels were prepared with various concentrations as shown in Table 1.

### 2.1. GelMA synthesis

GelMA was prepared using one-pot synthesis employing conditions optimized by Shirahama et al. [57] to obtain >95% degree of substitution of methacrylic anhydride (MAA). Briefly, gelatin 175 bloom was dissolved at 20 w/v% concentration in 0.25 M sodium bicarbonate buffer at pH 9 and 50 °C. Sodium biocarbonate buffer was prepared by dissolving 3.18 g sodium carbonate and 5.86 g sodium bicarbonate in 1 L deionized water and the pH was adjusted to 9 using 5 M sodium hydroxide or 6 M hydrochloric acid. Methacrylic anhydride (0.1 mL per gram of gelatin) was added dropwise while stirring at 600 rpm and allowed to react for 3 h, at which point the reaction was stopped by readjusting the pH to 7.4. The mixture was filtered using standard filter paper (qualitative) and membrane filter with 0.2 μm pore diameter. The solution was then dialyzed against distilled water using a 10 kDa molecular weight cut-off limit dialysis tube at 40 °C for 3 days. Functionalized gelatin solution was then lyophilized to generate a spongy foam which was stored at −20 °C until further use.

### 2.2. GelMA, Pluronic® and agar hydrogel preparation

Three different concentrations of hydrogels were prepared, 7.5%, 11.25% and 15% (w/v), by dissolving the lyophilized GelMA in Dulbecco's Modified Eagle Medium (DMEM, Thermo Fisher Scientific) containing 0.5% (w/v) photoinitiator, 2-hydroxy-1-(4(hydroxyethoxy) phenyl)-2 methyl-1 propanone (Irgacure-2959). Photo-curing of GelMA was achieved by using 360 nm UV lamp (Omnicure S1000, Alpha UV Systems) for 5 min. Pluronic® F127 at 40% (wt/v) in DMEM was

**Table 1**
Summary of all the used and retrieved parameters during the fit of the velocity profiles. For Agar and UV crosslinked GelMA (GelMA-gel), fluid parameters were indeterminate due to flat velocity profiles (refer to text).

| Hydrogel material | Concentration wt% | Average velocity μm $s^{-1}$ | Flow rate ml $h^{-1}$ | n | $\left(\frac{\Delta P_f}{2LK}\right)$ (μm $s^n)^{-1}$ |
|---|---|---|---|---|---|
| Uncrosslinked | 11.25 | 2256 | 1.02 | 0.946 | 0.16 |
| GelMA | 11.25 | 1739 | 0.79 | 0.804 | 0.081 |
| (GelMA-sol) | 7.5 | 508 | 0.23 | 1 | 0.053 |
| Pluronic® | 40 | 438 | 0.20 | 0.077 | 0.006 |
| Agar | 1 | 501 | 0.24 | – | – |
| UV crosslinked | 11.25 | 2199 | 0.99 | – | – |
| GelMA | 11.25 | 1548 | 0.70 | – | – |
| (GelMA-gel) | 11.25 | 1272 | 0.58 | – | – |
| | 11.25 | 408 | 0.18 | – | – |
| | 15 | 553 | 0.25 | – | – |
| | 7.5 | 488 | 0.22 | – | – |

prepared by dissolving Pluronic® powder in DMEM at 4 °C. Pluronic® at 40% is a gel at room temperature. Hence, processing was performed at 4 °C prior to extrusion. Agar (Sigma) was prepared at concentrations of 1% and 2% using phosphate-buffered saline (PBS).

### 2.3. Cell culture

Human osteosarcoma cell line, SaOS2 (ATCC, USA), was cultured in T75 flasks at a density of $2 \times 10^6$ cells $ml^{-1}$ in cell culture medium (Basic growth medium, McCoy). The medium was supplemented with 10% (v/v) fetal calf serum (Biosera), 0.297 g L-glutamine/500 ml bottle of media (Sigma), 1% penicillin–streptomycin (PS; 100 U $ml^{-1}$ penicillin, 0.1 mg $ml^{-1}$ streptomycin (Sigma), (Biosera)) and incubated at 37 °C in humidified 5% $CO_2$ incubator. The medium was changed twice a week until confluent cell monolayer was formed. The passage number of cells used in experiments was 12–15. Cells were then collected, counted, and stained with CellTracker Violet (2, 3, 6, 7- tetrahyfro-9-bromomethyl-1H, 5H-quinolozino-(9, 1-gh) coumarin, ThermoFisher) at 25 μM concentration. CellTracker Violet stained cell pellets were first resuspended in media then added to hydrogel solutions to a final concentration of 1 ×

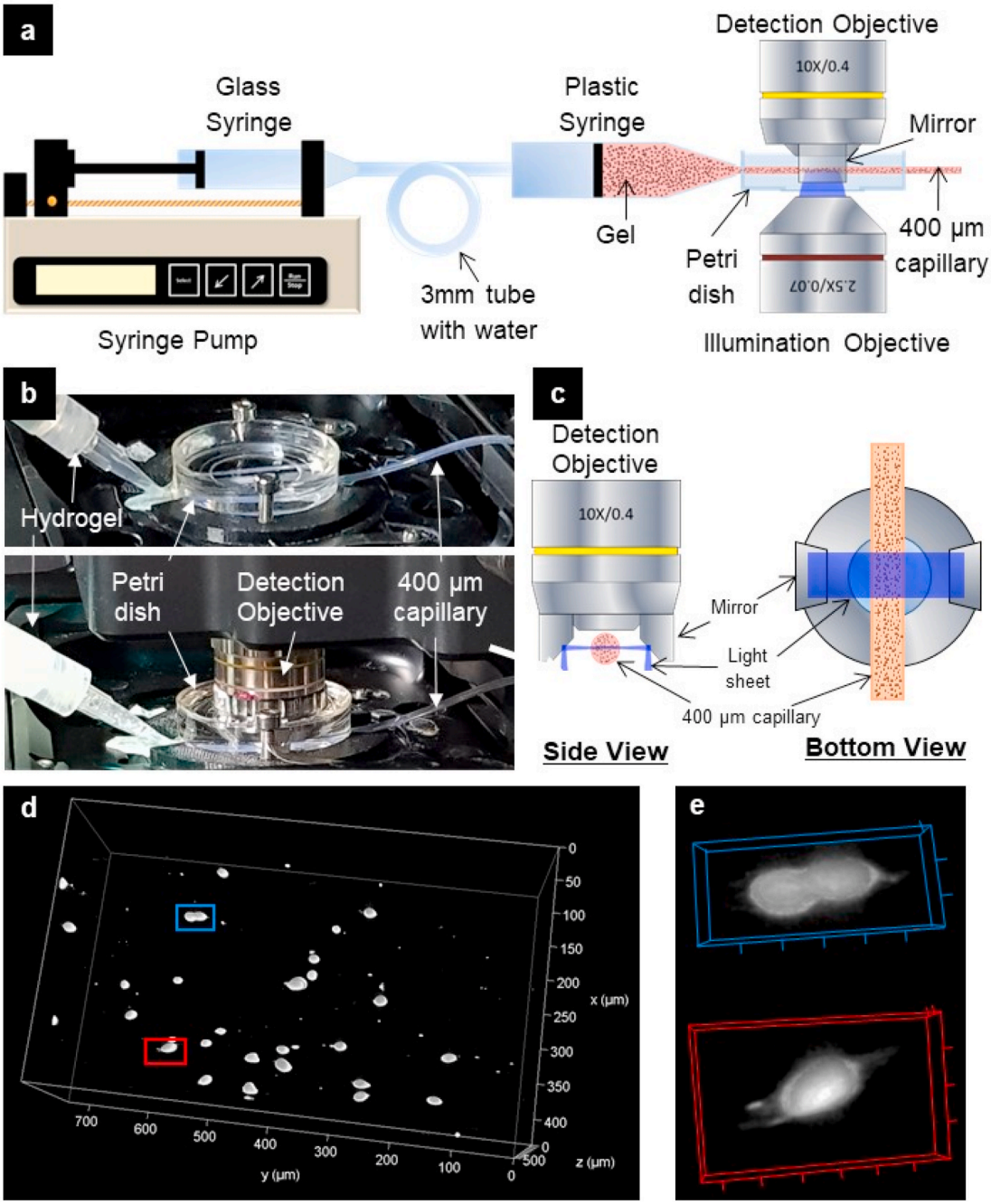


**Fig. 1.** (a–c) Light sheet fluorescence microscopy and extrusion setup used to perform real-time images of extrusion of cell laden hydrogels. Side and bottom view in (c) illustrate the light sheet configuration, showing the light sheet being created between the two mirrors across the width of the capillary and the detection objective placed perpendicular to the light sheet allowing low photo toxic 2D (midplane slice) and 3D images to be captured. Panel (d) shows a 3D reconstruction of the cells contained in the capillary, while panel (e) displays zoomed in cells from the blue and the red boxes highlighted in panel (d), underlining the ability to image cell morphology and processes with this technique. Ticks in (e) correspond to 10 μm. (For interpretation of the references to color in this figure legend, the reader is referred to the Web version of this article.)

$10^6$ cells $ml^{-1}$ and gently agitated to homogenize. In the case of Pluronic® cells were suspended at 4 °C to maintain hydrogel at low viscosity to allow homogeneous mixing.

### 2.4. Cell viability

SaOS2 cells encapsulated in the hydrogels (11.25 w/v% gelatin) were assessed using the LIVE/DEAD™ kit, for mammalian cells, (ThermoFisher). Bioinks were extruded through a 400 μm internal diameter clear capillary (fluorinated ethylene propylene (FEP); Adtech capillary) using a syringe pump (Cole-Parmer) and a glass syringe (Hamilton syringe 1001); and the extruded material collected in a petri-dish. GelMA bioinks were photo cured using a UV lamp (Omnicure S1000, Alpha UV Systems) set to a light intensity of 15 mW $cm^{-2}$ at 4.5 cm distance from the gel and used with an exposure time of 5 min. Cell viability of the cured then extruded (GelMA-gel) and extruded then cured (GelMA-sol) bioinks were compared to cast then cured bioinks following incubation for 3 and 24 h following manufacture's recommended protocol. Briefly, the gels were washed with PBS, stained with the LIVE/DEAD™ kit (1 μM EthD-I, 2 μM Calcein-AM) and incubated for 20 min at room temperature. After washing the samples with PBS, images were taken using a Zeiss LSM 700 confocal microscope. Live and dead cells were quantified using Fiji [58]. Cell viability was calculated as (number of green stained cells/number of total cells) × 100%.

### 2.5. LSFM imaging

The imaging experimental setup consists of two parts: the light-sheet fluorescence microscope (Leica SP8) [46,59] and the bioink extrusion system (Fig. 1a–c). This latter is composed of a syringe pump (Cole--Parmer), a glass syringe (Hamilton syringe 1001), and a tube connected to the gel extrusion syringe (disposable EFD Nordson luer-lock syringe). On activating the syringe pump, the bioinks flow through a 400 μm internal diameter clear plastic capillary (fluorinated ethylene propylene (FEP); Adtech capillary) representing the printing capillary in an extrusion bioprinter (Fig. 1a and b). To enable LSFM with a water immersion objective, the capillary is submerged in water inside a petri dish (35 mm glass bottom petri dish, Ibidi) and placed on the microscope stage. The hydrogels were extruded at flow rates between 0.2 and 10 ml $h^{-1}$ which covers the range typically used for bioprinting [28].

In the LSFM the illumination objective (HC PL FLUOTAR 2.5×/0.07 DRY) guides the 405 nm wavelength laser vertically to two mirrors attached over the detection objective (HC APOL 10×/0.30 water; Fig. 1c). By scanning the laser at 1400 Hz, a digital light sheet of 3.6 μm thickness is created in between the two mirrors horizontally, where the capillary is positioned. The detection objective positioned vertically above the capillary captures the emitted fluorescence which is band-pass filtered (455–495 nm) and then collected with a 2048 × 2048 pixel camera (Hamamatsu Flash 4 V2). The selected field of view is 735 μm × 420 μm, giving a pixel size of 0.359 μm.

### 2.6. Image acquisition and visualisation

For single-plane two-dimensional acquisitions, the middle plane of the capillary was imaged continuously. Images were recorded every 28 ms, with an exposure time of 10.6 ms. This imaging condition gave sufficient signal-to-noise to capture cells (Fig. 1d and e) and segment the labelled cells while reducing streaking artifacts from fast moving cells. A minimum of 5000 frames were collected per extrusion experiment.

Multi-slice 3D image datasets across the entire width of the extrusion capillary were acquired from 266 planes spaced 2 μm apart. The exposure time for a single plane was 7 ms, resulting in the acquisition of one volume dataset every 7.7 s, and a minimum of 10 vol were captured per extrusion condition.

Leica LAS X software was employed to produce the 3D rendering of the multi-slice 3D image datasets. The pixel classification tool Ilastik [60] was used to segment both 2D and 3D datasets based on the Random Forest algorithm and the output rendered on Fiji.

### 2.7. Analysis of light-sheet images

Fiji [58] plugin TrackMate [61], was used for cell detection and tracking across a minimum of 156 frames. The plugin is based on the Laplacian of Gaussian filter for spot detection and on Linear Assignment Problem for computing the tracks. The computed tracks contain information on the cell velocity as a function of time, which allows separation of different extrusion rates, and as a function of distance along the capillary which gives cell velocity profile in the capillary. It would also be possible to calculate cell velocity using a single frame when the phenomenon of streaks is visible by dividing the length of the streak by the exposure time. This approach could allow one to measure velocities up to 73 mm $s^{-1}$ (in contrast with velocity up to 25 mm $s^{-1}$ with the multiframe method) with the described setup, and even larger ones when using a lower magnification objective. However, this single-frame method is prone to inaccuracies due to variabilities in the cell dimensions or to presence of cell aggregates, and is further complicated by the low number of cells in a single frame. The multiframe method works well with cell concentrations of around $1 \times 10^6$ cells $ml^{-1}$ which leads to cells being distributed throughout the hydrogel such that they can be individually detected and tracked. Based on the spatial resolution of our setup we estimate that the concentration of cells may be increased by at least 40X without degrading the analysis.

A power-law fluid model was used to determine the deviation of each fluid from Newtonian behavior based on the measured velocity profiles. The measured velocity profiles were fit with the equation [62]:

$$v = \frac{n}{n+1}\left(\frac{\Delta P_f}{2LK}\right)^{\frac{1}{n}}\left(R^{\frac{n+1}{n}} - r^{\frac{n+1}{n}}\right) \quad (1)$$

where v is the flow velocity, $\Delta P_f$ is the pressure drop across the length of the capillary L, r is radial position, R is the radius of the capillary, and K and n are the flow consistency index and the flow behavior index, respectively, from the power law relationship

$$\tau = K\left(\frac{dv}{dr}\right)^n \quad (2)$$

where τ is the r-z component of the viscous stress tensor. For a Newtonian fluid, n = 1, and K would be the dynamic viscosity. Given the almost certainly reliable assumption of Poiseuille flow conditions (the Reynolds numbers are estimated at <10), the fluid can be described shear thickening if $n > 1$, or shear thinning if $n < 1$ [62]. Shear-thinning fluids may also exhibit a yield stress, but employing such a model would require a more accurate assessment of the yield stress than is obtainable with this method. By iteratively fitting the experimental velocity profiles to equation [1] on MATLAB® with a least squares method, the values for n and ($\Delta P_f$/2LK) were obtained. Additionally, the shear rate profile can be obtained by derivation of the velocity with respect to the radius [62]. The volumetric flow rate (Q) was calculated as the product of the average flow velocity and the cross-sectional area of the capillary. We have limited our investigations to the observation of cell and fluid movements in the capillary. A full assessment of bioink properties and other parameters such as the shear stress to which the cells were subjected would require additional measurements such as the pressure within the syringe and/or separate bioink viscometry.

## 3. Results and discussion

### 3.1. Cell extrusion and flow velocity profiles

Light sheet fluorescence microscopy (LSFM) was employed to quantify flow of cell-laden hydrogels through a capillary in real-time to

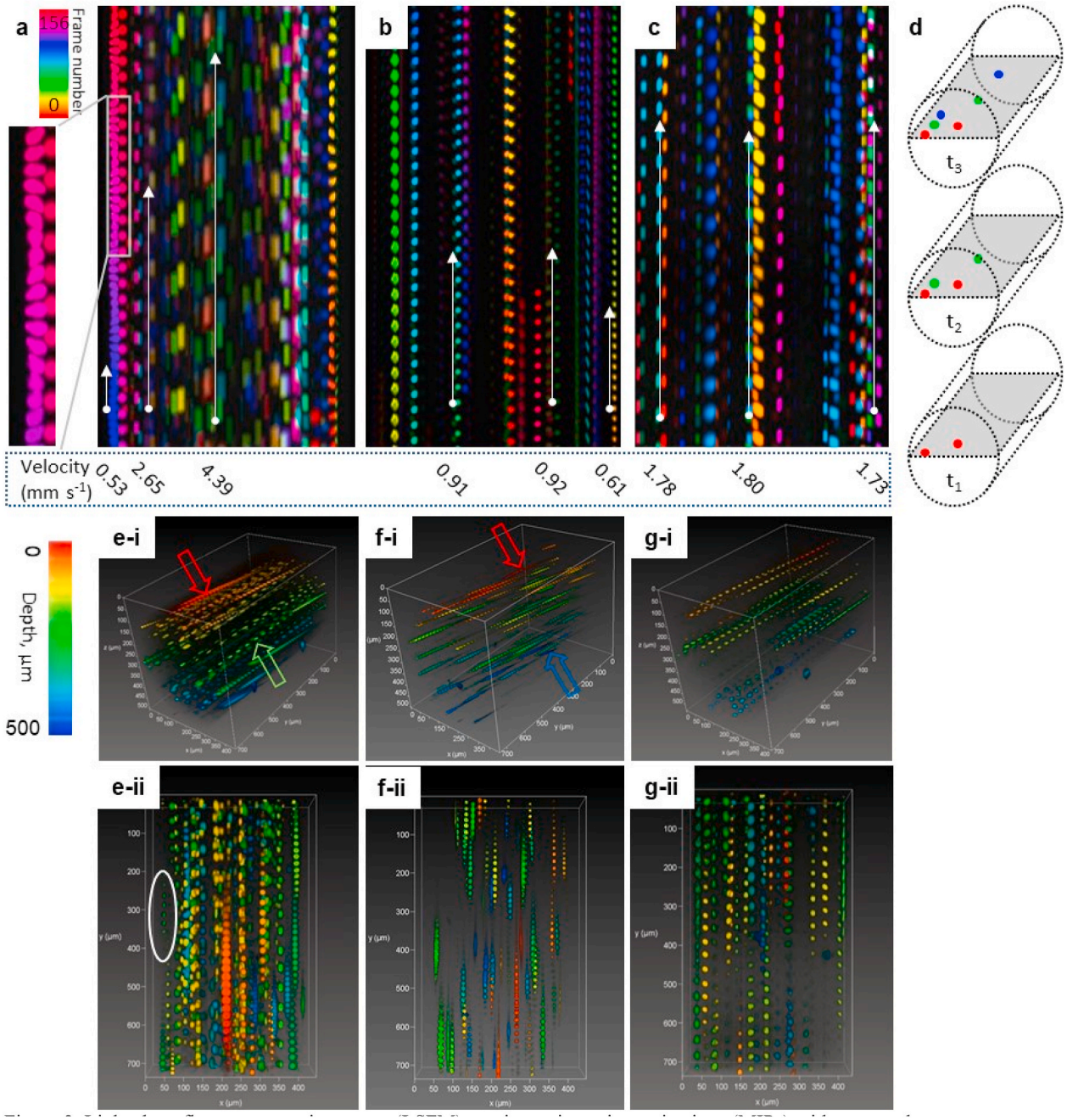


**Fig. 2.** Light sheet fluorescence microscopy (LSFM) maximum intensity projections (MIPs) with temporal color-coding of the midplane of the capillary while flowing (a) uncrosslinked GelMA (GelMA-sol), (b) Pluronic® and (c) UV crosslinked GelMA (GelMA-gel) bioinks. (d) Schematic to demonstrate the formation of the temporal color codes used in the MIPs, where two cells in the image frame with different velocities at 3 consecutive time-point t1, t2 and t3 are colored differently (see legend in a). Direction of flow in (a–c) is bottom to top and the white arrows indicate the distance covered by cells in fixed unit of time at various locations in the capillary. The expanded region in (a) shows cells closer to the capillary wall, where the cells can be observed to rotate anticlockwise. (e–g) 3D reconstructions of stacks acquired during the flow of (e) GelMa-sol, (f) Pluronic® and (g) GelMA-gel. Color code is representative of the depth. Red and green arrows in (e–i) points to cells close to the wall and center of the capillary, respectively. Whilst arrows in f-i points to cells on the wall of the capillary. The white circle in (e-ii) highlights a cell rotating anti-clockwise where the flow direction is bottom to top. (For interpretation of the references to color in this figure legend, the reader is referred to the Web version of this article.)

provide information on cell-hydrogel interplay within a mimic of extrusion bioprinting process (Fig. 1d and e). LSFM of fluorescently labelled cells yielded capillary flow profiles for various bioinks studied (Fig. 2). Fiji plugin Trackmate was used to detect and track cells (Fig. 3a–c) and the velocity of cells flowing through the capillary were quantified to output the fluid flow profiles (Fig. 3e and f). Capillary velocity profiles were consistent with Poiseuille flow for the uncrosslinked GelMA bioink solution (GelMA-sol), and blunted velocity profiles for the Pluronic® and UV crosslinked GelMA (GelMA-gel) (Figs. 2 and 3h-m). The reconstructed cell trajectories color coded accordingly to the mean velocity for GelMA-sol, Pluronic® and GelMA-gel are shown in Fig. 3h–j. Cells in GelMA-sol at the center of the capillary exhibited the highest flow velocities (Fig. S1a, Supporting Information) and a parabolic velocity profile. In the center, the cells appear elongated (or streaked, Fig. 2a) due to the flow speed of the cell exceeding the ratio of field of view to exposure time. Near the capillary

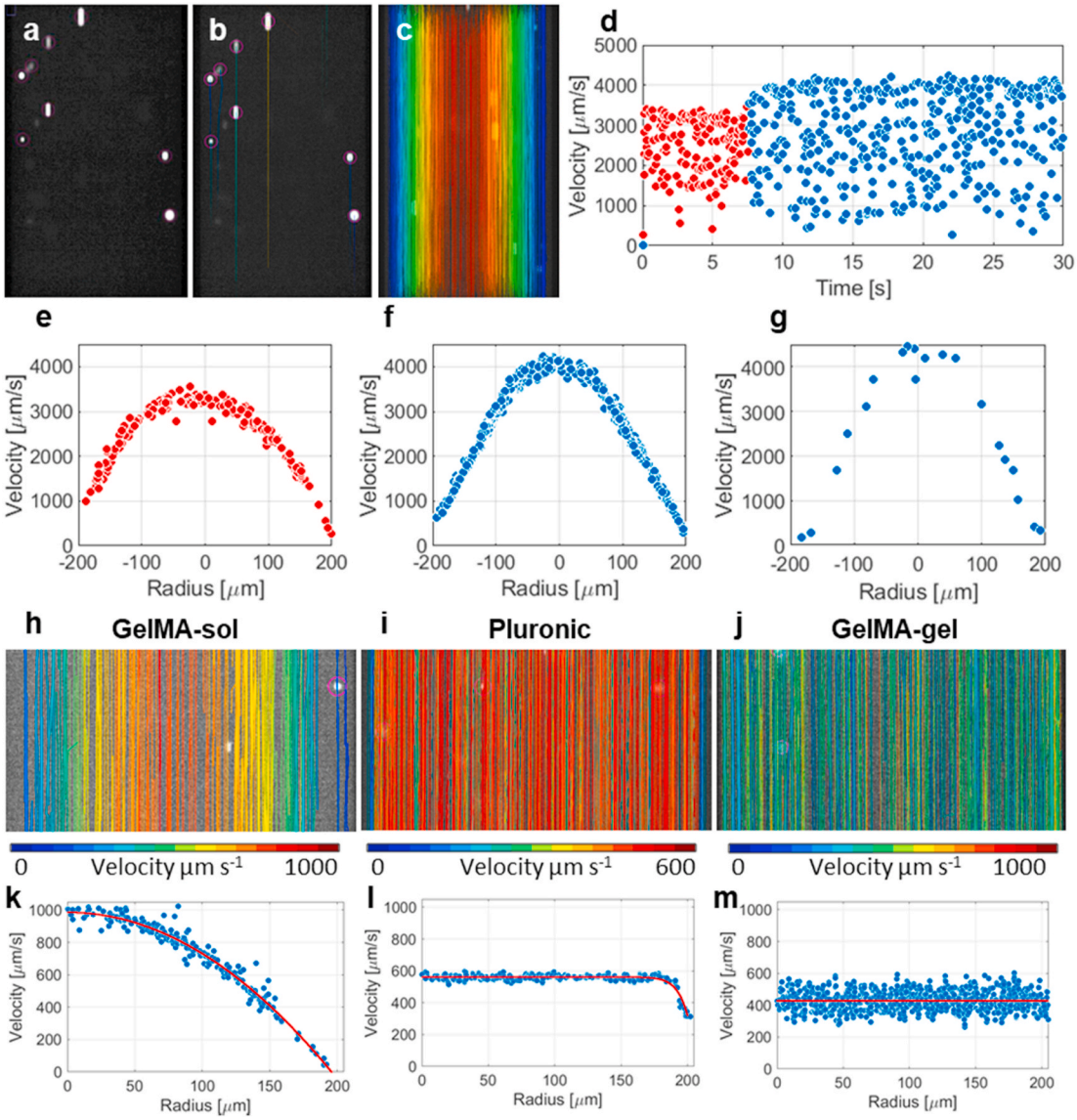


**Fig. 3.** Cell tracking and analysis of the velocity profiles. (a) Example of a midplane image obtained from the light sheet experiment while extruding 11.25 wt% GelMA-sol. (b) The Laplacian of Gaussian (LoG) spot detection algorithm with 30 μm "blob" detection was applied to detect the cells after a threshold was set. Cells were then tracked using a Linear Assignment Problem (LAP) mathematical formulation, and each tracks were color coded based on the velocity of the cells and (c, h-j) overlaid. (d) The velocity of each detected cell was extracted and plotted as a function of time to separate the different extrusion speeds applied (red and blue dots). This was then followed by each velocity plotted as a function of position for the various velocities, here, red identifies first extrusion rate (e) and blue the second (f). Alternatively, cell velocity could be calculated from streaks formed by the cells in a single frame using particle streak velocimetry. This is shown in (g) for the same extrusion rate as in (f). Panels (h–j) shows the extracted cell tracks overlaid for (h) GelMA-sol, (i) Pluronic®, and (j) GelMA-gel. The color coding is representative of the calculated mean velocities given in μm $s^{-1}$. Panels (k–m) shows plot of tracked cell velocities and the fitting based on Equation (1) (see Section 2.7) to estimate the fluid velocity profile as a function of the distance from the center of the capillary for (k) GelMA-sol, (l) Pluronic® and (m) GelMA-gel. (For interpretation of the references to color in this figure legend, the reader is referred to the Web version of this article.)

wall, where the cell velocities are relatively slow, the cell shape is resolved more clearly. Here, some cells can be seen to roll on the surface of the capillary (Fig. 2a expanded region) whilst those in the vicinity, but not in contact with the wall, are seen to spin, with the ones closer to the center rotating less obviously due to the faster forward movement (Fig. S1b, Supporting Information). Rotation of the cells is clockwise on the right side and anti-clockwise on the left side of the capillary. 3D reconstructions confirmed axisymmetric flow and these cell behaviors (Fig. 2e and S2, Supporting Information). GelMA-sol with cells suspended at $10^6$ cells $ml^{-1}$ concentration still behaves as a Newtonian fluid, exhibiting a parabolic velocity profile (Fig. 3k), similarly to the flow of dilute suspensions of red blood cells through channels >100 μm diameter [39]. Flow of the Pluronic® gel in the capillary exhibited a uniform cell velocity ('plug flow') across most of the diameter, with cell velocity decreasing near the capillary wall (Fig. 2b,f, 3i,l and S3, Supporting Information). Meanwhile, the GelMA-gel appears to have a uniform velocity throughout the capillary cross-section (Fig. 2c,g 3j,m, S4 and S5, Supporting Information), but with 4 times the variations in velocity compared to Pluronic® and GelMA-sol (Fig. 3k-m).

Fluid behavior was quantified by fitting the velocity profiles (Fig. 3k-m) with the fluid mechanics model given by Equation (1) in section 2.7. GelMA-sol exhibited a parabolic flow profile, fitting the velocity profile yielded a flow behavior index n of between 0.8 and 1 (Table 1) suggesting that the GelMA-sol behaves as a Newtonian fluid. In contrast, the plug flow profile for Pluronic® (Figure 3l) yielded n of less than 0.08, indicating a non-Newtonian, shear thinning fluid, similar to previous

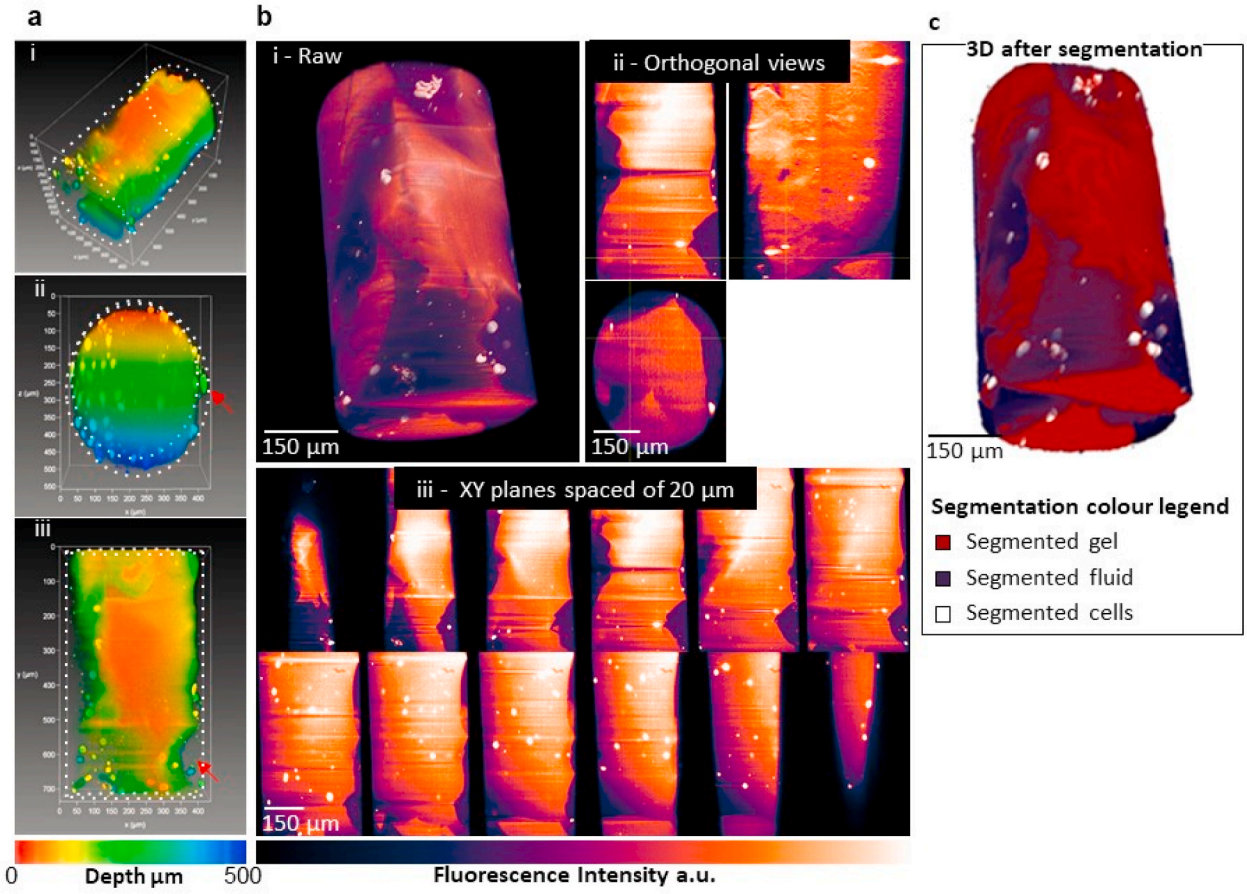


**Fig. 4.** Fracture morphologies of the UV crosslinked GelMA bioink in the capillary. (a) Three-dimensional reconstruction of the bioink with cells embedded within it. Color coding represents depth, where red is the top layer and blue the bottom. The hydrogel does not fill the entire capillary, with cells that can be observed within the gel and in fluid regions. The dotted lines represent the outline of the capillary wall. The red arrow points towards a void filled with media where a cell has been trapped. (b) 3D rendering of the raw fluorescence intensity (bi), orthogonal views (bii), and XY planes (biii) taken every 20 µm from the acquired stack; in this case colours are representative of fluorescence intensity, where the cells appear white since they have the highest fluorescence, the voids appear black-purple and the bioink has a false colour ranging from purple to orange to white. A highly fractured gel morphology is observed. (c) 3D reconstruction of the same sample after segmentation performed with Ilastik, a pixel classifier based on the Random Forest algorithm. The cells are in white, the fluid in purple and the bioink in magenta. The fluid portion represents 13% of the overall volume. (For interpretation of the references to color in this figure legend, the reader is referred to the Web version of this article.)

observations [24,63]. Because the LSFM method relies on detection of cells to obtain velocity, it was unable to resolve the near-wall fluid shear layer for the GelMA-gel (Fig. 3m and S6a–c, Supporting Information) and agar (Fig. S6d, Supporting Information) therefore fitting the data to Equation (1) gives no valid solution for n.

The approach presented here constitutes a version of capillary viscometry where rather than measuring time taken for a fixed volume of fluid to flow through the capillary, we deduce fluid flow profiles and behavior directly from real-time imaging. This method of viscometry has the advantage of assessing fluid behavior in the actual flow situation of interest to facilitate the understanding of the mechanisms underlying differences in cell viability. While we have not verified the accuracy of this viscometry method, the flow behavior index calculated for the various materials is in close agreement to published literature employing rotational viscometry. Paxton et al. [24] and Suntornnond et al. [63] report flow behavior index for 25 w/v% Pluronic® to vary between 0.127 and 0.051, respectively. The value calculated here (0.077) falls within this range. It should be noted that the approach presented here should be performed in addition to a full assessment of bioink properties and other parameters such as the shear stress using an oscillatory viscometry.

### 3.2. Bioink flow and its morphology within the capillary

The autofluorescence of GelMA-gel made it possible to image the hydrogel itself in the capillary (Fig. 4 and S7, Supporting Information). There were numerous observable discontinuities in the GelMA-gel, indicating a separation of solid and fluid phases (Fig. 4, S7, S8 and S9, Supporting Information). Cells were present in both phases and those embedded in the solid phase move coincidentally with the hydrogel, while the cells in the fluid phases were observed to swirl and spin due to local motion of the fluid where the cells are located (Fig. S9, Supporting Information). The multiphase behavior results in irregularly shaped solid phases suspended in fluid, and explains the variation in velocity measurements (Fig. 3m). As illustrated in Fig. 5 Pluronic® exhibits a yield stress shear thinning flow [64] and has a homogeneous gel morphology while GelMA-gel displays an inhomogeneous fractured flow. It also appears in Fig. 3m that the GelMA-gel velocity at the wall is finite, but this is a result of using cell velocity for fluid flow estimation which does not capture the successive passing of both fluid (at the capillary wall) and solid phases in the sampling area. However, there is always a thin layer of fluid separating the solid phase from the wall [65, 66], as occurs with microgel-liquid systems [67–69]. The thin (few molecular diameter to sub-micrometer) liquid layer lubricates the space between the wall and the gel [70], therefore both Pluronic® and

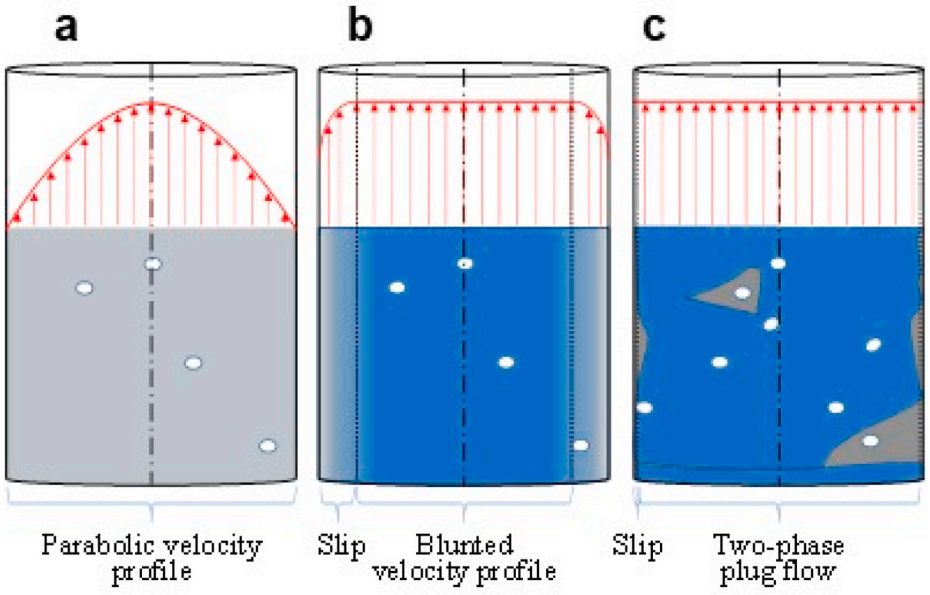


**Fig. 5.** Shows schematics of the fluid behavior in the (a) Newtonian, (b) yield stress or shear-thinning fluid and (c) 'over-gelled' bioinks.

GelMA-gel appear to have a finite velocity (slip velocity) at the capillary wall as illustrated in Fig. 5b and c, respectively. The fluid phase at the wall in the GelMA-gel is much more exaggerated (Fig. 4, S7 and S8, Supporting Information) due to its fractured morphology, this contributes to a pure plug flow with constant velocity throughout the capillary. The fractured morphology of the GelMA-gel, is likely a result of the forces encountered in the converging region upstream of the capillary and shear stress along the capillary wall, resembles that of polyethylene melt extrudate [32,71]. On average a fluid volume of ~13% was calculated over the entire cross-section of the capillary for the 11.25% GelMA-gel as a result of gel fracturing. Similar fractured morphology and flow behavior was observed for all the concentrations of GelMA-gel (7.5%, 11.25% and 15%, Table 1) and agar (Fig. S10, Supporting Information).

Gel fracturing during printing of 'over-gelled' bioinks diminishes the mechanical integrity of the printed constructs therefore is important to characterize. LSFM-based real-time imaging was key in shedding light on the real flow behavior of complex fluids, and their influence on cells, in addition to the calculation of flow profiles (see section 3.1). Furthermore, such information can also be coupled with mathematical models of extrusion bioprinting [15,17–19,21–23,63] to refine the design of injection protocols and hydrogel property specification to improve printing outcomes.

### 3.3. *Effect of bioink and extrusion parameters on cell viability*

Cell (SaOS2) viability was highest (>90%) in the control group (GelMA-cast and non-extruded). Cells extruded with GelMA-gel showed better cell viability compared to GelMA-sol at 3 and 24 h (Fig. 6). However, in both cases cell viability is higher at 3 h compared to 24 h after extrusion. Within the extruded groups, higher flow rates also reduce cell viability. Survival rates were about 2 and 2.25 times lower when extruding at speeds of 10 ml $h^{-1}$ compared to extruding at 1 or 5 ml $h^{-1}$, respectively. Shear thinning behavior in hydrogels has previously been reported to protect cells from mechanically-induced lysis, giving higher cell viability rates than when Newtonian fluids were used [15,72]. The data presented here suggest that the GelMA-gel flow patterns also lead to better cell viability compared to the flow of the Newtonian GelMA-sol. However, the reduction in cell viability from 3 h to 24 h even at the slowest extrusion speed (1 ml $h^{-1}$) suggests further optimization of bioinks and bioprinting is required to minimize accumulation of damage. Another potential factor that could have contributed to reduced cell viability at 24 h compared to 3 h is the limited oxygen exchange to the cells encapsulated in the printed hydrogels, which is influenced by the hydrogel structure and properties [73]. Large concentration of GelMA (>30 w/v%) in the hydrogels have been shown to adversely influence cell viability [74], our measurements show that the hydrogel flow patterns are similar for GelMA concentrations up to 11.25 w/v%, suggesting that the cell death from extrusion-induced mechanical damage will not be influenced by concentration at least within this range of GelMA concentration. Cell type and density will also significantly influence cell viability as different cells have different levels of tolerance to mechanical damage [75]. Furthermore, mathematical models should take into account near-wall fluid behavior and gel fracturing via appropriate fluid property specification, as these phenomena could have significant effect on cell damage.

## 4. Conclusions

Success and adoption of extrusion bioprinting relies on the ability to maintain cell viability through a narrow capillary onto a platform. This study demonstrates the power of light sheet fluorescence microscopy-based 3D real-time imaging to give new insights on cell and fluid movements and flow patterns during extrusion using different bioinks. Previous studies of flow behavior and mechanical stress on cells during printing lacked this information on cell dynamics, and often made faulty assumptions about fluid behavior and flow modeling. This manuscript provides the first experimental data for the flow of bioinks through a narrow capillary and deduced the flow behavior as indicative of Newtonian (uncrosslinked GelMA-sol), yield stress shear thinning (Pluronic®) or two-phase (UV crosslinked GelMA-gel and agar) fluids, based on the different velocity profiles. The approach presented in this study could lead to the development of novel designs of capillaries with complex structures and surface chemistry to modulate cell viability during extrusion bioprinting. Furthermore, the approach could aid in the development of new bioinks to facilitate flow through the capillary and enhance cell viability and thus the success of bioprinting. Potential future research directions toward this overall goal include applying our techniques to rectangular, conical and patterned printing needles, different needle materials to modulate needle surface chemistry (noting the requirement for optical clarity), plus variations in cell type and

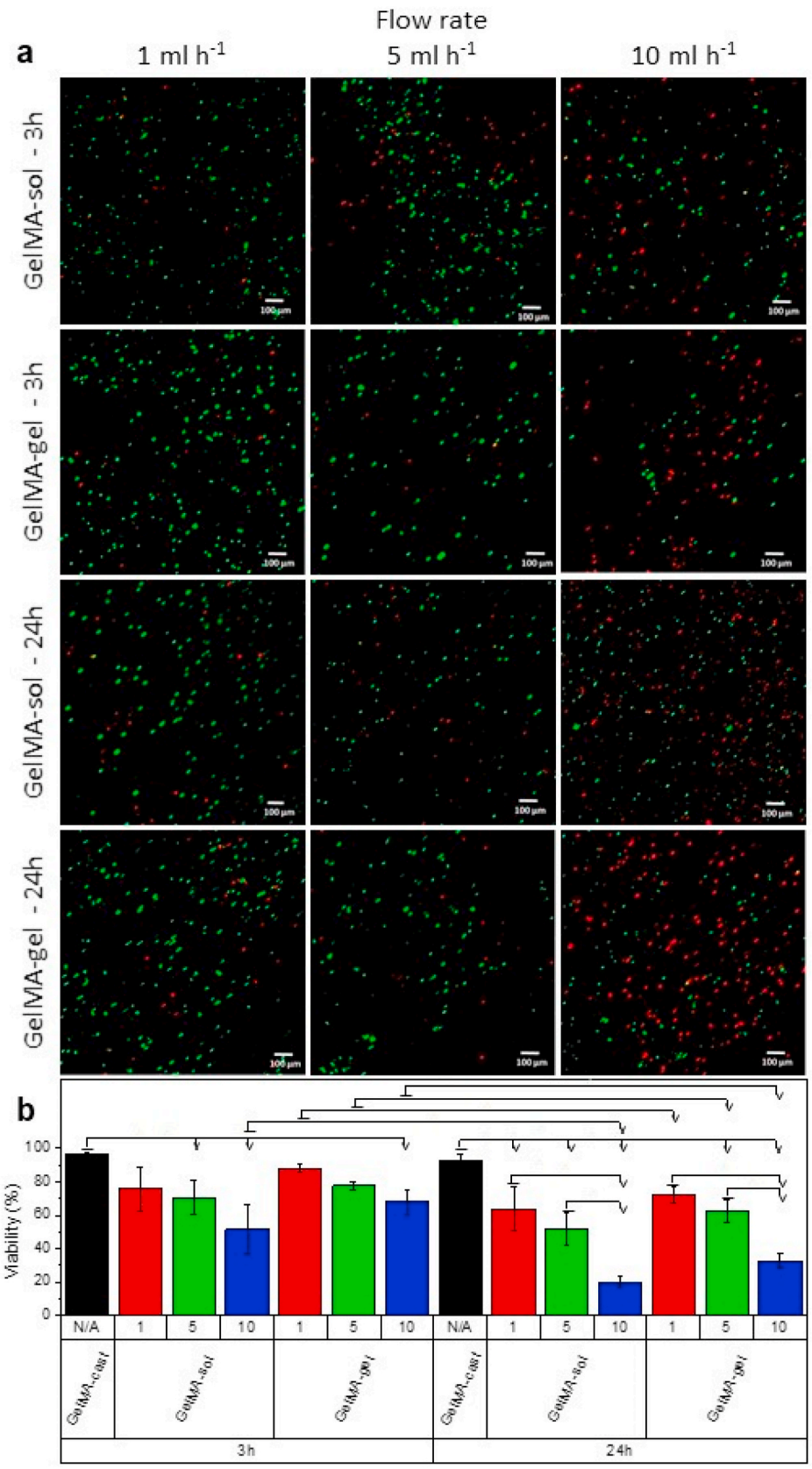


**Fig. 6.** (a) Confocal images from cell viability LIVE/DEAD assay for uncrosslinked GelMA (GelMA-sol) and UV crosslinked GelMA (GelMA-gel) after 3 h and 24 h extrusion at various flow rates (1, 5 and 10 ml $h^{-1}$). Live and dead cells are labelled green and red, respectively; scale bars 100 µm. b) Viability quantified as percentage of live cells over all cells is plotted for the hydrogels extruded at various flow rates (cast-N/A, 1, 5 and 10 ml $h^{-1}$) grouped by the various hydrogel processing (GeMA-cast, GelMA-sol or GelMA-gel) and period of cell culture (3h or 24h). Error bars are standard deviations. Significant differences within specimen groups are identified on the plots with brackets where $p < 0.05$ calculated by performing one-way ANOVAs and post-hoc Tukey comparisons. (For interpretation of the references to color in this figure legend, the reader is referred to the Web version of this article.)

density. Moreover, our approach may also spark the development of imaging for application to process monitoring thus contributing to standardization and regulatory approval of bioprinted constructs.

## CRediT authorship contribution statement

**Gowsihan Poologasundarampillai:** Conceptualization, Methodology, Resources, Writing – review & editing, Resources, Funding acquisition, Visualization, Supervision. **Abdelrahman Haweet:** Formal analysis, Investigation, Writing – original draft. **Soher Nagi Jayash:** Methodology, Investigation, Formal analysis. **George Morgan:** Investigation, Writing – review & editing. **James E. Moore:** Methodology, Validation, Investigation, Writing – review & editing, Supervision. **Alessia Candeo:** Conceptualization, Methodology, Resources, Writing – review & editing, Resources, Funding acquisition, Visualization, Supervision.

## Declaration of competing interest

The authors declare that they have no known competing financial interests or personal relationships that could have appeared to influence the work reported in this paper.

## Acknowledgements

This study was made possible thanks to funding from EPSRC (grant number EP/M023877/1) and STFC-Central Laser Facility (LSF REF No: 17330041). Light Sheet Fluorescence was performed at the OCTOPUS imaging cluster at the Central Laser Facility located at the Research Complex at Harwell, UK. Special thanks to Cara Foundation and University of Birmingham for supporting Soher Jayash as Post-Doctoral Fellow in the University of Birmingham. The mobility of author Abdelrahman Haweet was possible with the support of the European Union Erasmus+ scheme. James Moore acknowledges the support of Bagrit Chair. The authors would like to acknowledge Chrisoula Chappel for supplying GelMA and Lamis Elsawah for reviewing the manuscript. Raw data requests to the authors for analysis and modeling applications are encouraged.

## Appendix A. Supplementary data

Supplementary data to this article can be found online at https://doi.org/10.1016/j.bprint.2021.e00144.

## References

[1] L. Moroni, J.A. Burdick, C. Highley, S.J. Lee, Y. Morimoto, S. Takeuchi, et al., Biofabrication strategies for 3D in vitro models and regenerative medicine, Nature Rev. Mater. 3 (5) (2018) 21–37.
[2] F.P.W. Melchels, M.A.N. Domingos, T.J. Klein, J. Malda, P.J. Bartolo, D. W. Hutmacher, Additive manufacturing of tissues and organs, Prog. Polym. Sci. 37 (8) (2012) 1079–1104.
[3] A.M. Jorgensen, J.J. Yoo, A. Atala, Solid organ bioprinting: strategies to achieve organ function, Chem. Rev. 120 (19) (2020) 11093–11127.
[4] I.T. Ozbolat, M. Hospodiuk, Current advances and future perspectives in extrusion-based bioprinting, Biomaterials 76 (2016) 321–343.
[5] M.E. Prendergast, J.A. Burdick, Recent advances in enabling technologies in 3D printing for precision medicine, Adv. Mater. 32 (13) (2020), 1902516.
[6] N. Noor, A. Shapira, R. Edri, I. Gal, L. Wertheim, T. Dvir, 3D printing of personalized thick and perfusable cardiac patches and hearts, Adv. Sci. 6 (11) (2019), 1900344.
[7] D.B. Kolesky, R.L. Truby, A.S. Gladman, T.A. Busbee, K.A. Homan, J.A. Lewis, 3D bioprinting of vascularized, heterogeneous cell-laden tissue constructs, Adv. Mater. 26 (19) (2014) 3124–3130.
[8] S. Ramesh, Y. Zhang, D.R. Cormier, I.V. Rivero, O.L. Harrysson, P.K. Rao, et al., Extrusion bioprinting: recent progress, challenges, and future opportunities, Bioprinting (2020), e00116.
[9] K. Hölzl, S. Lin, L. Tytgat, S. Van Vlierberghe, L. Gu, A. Ovsianikov, Bioink properties before, during and after 3D bioprinting, Biofabrication 8 (3) (2016), 032002.
[10] M. Guvendiren, J. Molde, R.M.D. Soares, J. Kohn, Designing biomaterials for 3D printing, ACS Biomater. Sci. Eng. 2 (10) (2016) 1679–1693.
[11] S.M. Peltola, F.P.W. Melchels, D.W. Grijpma, M. Kellomäki, A review of rapid prototyping techniques for tissue engineering purposes, Ann. Med. 40 (4) (2008) 268–280.
[12] E.S. Bishop, S. Mostafa, M. Pakvasa, H.H. Luu, M.J. Lee, J.M. Wolf, et al., 3-D bioprinting technologies in tissue engineering and regenerative medicine: current and future trends, Genes Dis 4 (4) (2017) 185–195.
[13] M.L. Bedell, A.M. Navara, Y. Du, S. Zhang, A.G. Mikos, Polymeric systems for bioprinting, Chem. Rev. 120 (19) (2020) 10744–10792.
[14] R. Chang, J.W.S. Nam, Effects of dispensing pressure and nozzle diameter on cell survival from solid freeform fabrication–based direct cell writing, Tissue Eng. 14 (1) (2008) 41–48.
[15] B.A. Aguado, W. Mulyasasmita, J. Su, K.J. Lampe, S.C. Heilshorn, Improving viability of stem cells during syringe needle flow through the design of hydrogel cell carriers, Tissue Eng. 18 (7–8) (2012) 806–815.
[16] S. Boularaoui, G. Al Hussein, K.A. Khan, N. Christoforou, C. Stefanini, An overview of extrusion-based bioprinting with a focus on induced shear stress and its effect on cell viability, Bioprinting (2020), e00093.
[17] J. Snyder, A. Rin Son, Q. Hamid, C. Wang, Y. Lui, W. Sun, Mesenchymal stem cell printing and process regulated cell properties, Biofabrication 7 (4) (2015), 044106.
[18] K. Nair, M. Gandhi, S. Khalil, K.C. Yan, M. Marcolongo, K. Barbee, et al., Characterization of cell viability during bioprinting processes, Biotechnol. J. 4 (8) (2009) 1168–1177.
[19] T. Billiet, E. Gevaert, T. De Schryver, M. Cornelissen, P. Dubruel, The 3D printing of gelatin methacrylamide cell-laden tissue-engineered constructs with high cell viability, Biomaterials 35 (1) (2014) 49–62.
[20] L Lucas, A Aravind, P Emma, M Christophe, C Edwin-Joffrey, Rheology, simulation and data analysis toward bioprinting cell viability awareness, Bioprinting (2021) e00119.
[21] A. Blaeser, D.F. Duarte Campos, U. Puster, W. Richtering, M.M. Stevens, H. Fischer, Controlling shear stress in 3D bioprinting is a key factor to balance printing resolution and stem cell integrity, Adv. Healthcare Mater. 5 (3) (2016) 326–333.
[22] L. Ouyang, R. Yao, Y. Zhao, W. Sun, Effect of bioink properties on printability and cell viability for 3D bioplotting of embryonic stem cells, Biofabrication 8 (3) (2016), 035020.
[23] S.J. Müller, E. Mirzahossein, E.N. Iftekhar, C. Bächer, S. Schrüfer, D.W. Schubert, et al., Flow and hydrodynamic shear stress inside a printing needle during biofabrication, PloS One 15 (7) (2020), e0236371.
[24] N. Paxton, W. Smolan, T. Böck, F. Melchels, J. Groll, T. Jungst, Proposal to assess printability of bioinks for extrusion-based bioprinting and evaluation of rheological properties governing bioprintability, Biofabrication 9 (4) (2017), 044107.
[25] R.G. Larson, The Structure and Rheology of Complex Fluids, Oxford university press, New York, 1999.
[26] W. Wu, A. DeConinck, J.A. Lewis, Omnidirectional printing of 3D microvascular networks, Adv. Mater. 23 (24) (2011) H178–H183.
[27] W. Liu, M.A. Heinrich, Y. Zhou, A. Akpek, N. Hu, X. Liu, et al., Extrusion bioprinting of shear-thinning gelatin methacryloyl bioinks, Adv. Healthcare Mater. 6 (12) (2017), 1601451.
[28] L. Ouyang, C.B. Highley, C.B. Rodell, W. Sun, J.A. Burdick, 3D printing of shear-thinning hyaluronic acid hydrogels with secondary cross-linking, ACS Biomater. Sci. Eng. 2 (10) (2016) 1743–1751.
[29] L. Ouyang, C.B. Highley, W. Sun, J.A. Burdick, A generalizable strategy for the 3D bioprinting of hydrogels from nonviscous photo-crosslinkable inks, Adv. Mater. 29 (8) (2017), 1604983.
[30] M.H. Chen, L.L. Wang, J.J. Chung, Y.-H. Kim, P. Atluri, J.A. Burdick, Methods to assess shear-thinning hydrogels for application as injectable biomaterials, ACS Biomater. Sci. Eng. 3 (12) (2017) 3146–3160.
[31] L.E. Bertassoni, J.C. Cardoso, V. Manoharan, A.L. Cristino, N.S. Bhise, W.A. Araujo, et al., Direct-write bioprinting of cell-laden methacrylated gelatin hydrogels, Biofabrication 6 (2) (2014), 024105.
[32] M.M. Denn, Extrusion instabilities and wall slip, Annu. Rev. Fluid Mech. 33 (1) (2001) 265–287.
[33] A. Skardal, Perspective:"Universal" Bioink Technology for Advancing Extrusion Bioprinting-Based Biomanufacturing, Elsevier, 2018.
[34] R.J. Adrian, Particle-imaging techniques for experimental fluid-mechanics, Annu. Rev. Fluid Mech. 23 (1991) 261–304.
[35] J.G. Santiago, S.T. Wereley, C.D. Meinhart, D.J. Beebe, R.J. Adrian, A particle image velocimetry system for microfluidics, Exp. Fluid 25 (4) (1998) 316–319.
[36] H. Li, B. Huang, M. Wu, Experimental and numerical investigations on the flow characteristics within hydrodynamic entrance regions in microchannels, Micromachines 10 (5) (2019) 317.
[37] M.K. Raj, S. Bhattacharya, S. DasGupta, S. Chakraborty, Collective dynamics of red blood cells on an in vitro microfluidic platform, Lab Chip 18 (24) (2018) 3939–3948.
[38] V. Leble, R. Lima, R. Dias, C. Fernandes, T. Ishikawa, Y. Imai, et al., Asymmetry of red blood cell motions in a microchannel with a diverging and converging bifurcation, Biomicrofluidics 5 (4) (2011) 15.
[39] R. Lima, T. Ishikawa, Y. Imai, M. Takeda, S. Wada, T. Yamaguchi, Measurement of individual red blood cell motions under high hematocrit conditions using a confocal micro-PTV system, Ann. Biomed. Eng. 37 (8) (2009) 1546–1559.
[40] R. Lima, S. Wada, K-i Tsubota, T. Yamaguchi, Confocal micro-PIV measurements of three-dimensional profiles of cell suspension flow in a square microchannel, Meas. Sci. Technol. 17 (4) (2006) 797.
[41] G.E. Elsinga, F. Scarano, B. Wieneke, B.W. van Oudheusden, Tomographic particle image velocimetry, Exp. Fluid 41 (6) (2006) 933–947.
[42] D.H. Doh, G.R. Cho, Y.H. Kim, Development of a tomographic PTV, J. Mech. Sci. Technol. 26 (12) (2012) 3811–3819.

[43] C. Cierpka, C.J. Kähler, Particle imaging techniques for volumetric three-component (3D3C) velocity measurements in microfluidics, J. Visual 15 (1) (2012) 1–31.
[44] C. Liu, K. Kiger, Multi-camera PIV imaging in two-phase flow for improved dispersed-phase concentration and velocity calculation, Bull. Am. Phys. Soc. 60 (2015).
[45] H. Siedentopf, R. Zsigmondy, Uber sichtbarmachung und größenbestimmung ultramikoskopischer teilchen, mit besonderer anwendung auf goldrubingläser, Ann. Phys. 315 (1) (1902) 1–39.
[46] A.H. Voie, D. Burns, F. Spelman, Orthogonal-plane fluorescence optical sectioning: three-dimensional imaging of macroscopic biological specimens, J. Microsc. 170 (3) (1993) 229–236.
[47] J. Huisken, J. Swoger, F. Del Bene, J. Wittbrodt, E.H. Stelzer, Optical sectioning deep inside live embryos by selective plane illumination microscopy, Science 305 (5686) (2004) 1007–1009.
[48] P.J. Keller, A.D. Schmidt, J. Wittbrodt, E.H. Stelzer, Reconstruction of zebrafish early embryonic development by scanned light sheet microscopy, Science 322 (5904) (2008) 1065–1069.
[49] B.-C. Chen, W.R. Legant, K. Wang, L. Shao, D.E. Milkie, M.W. Davidson, et al., Lattice light-sheet microscopy: imaging molecules to embryos at high spatiotemporal resolution, Science 346 (6208) (2014).
[50] M. Weber, M. Mickoleit, J. Huisken, Light sheet microscopy, Methods Cell Biol. 123 (2014) 193–215.
[51] O.E. Olarte, J. Andilla, E.J. Gualda, P. Loza-Alvarez, Light-sheet microscopy: a tutorial, Adv. Opt. Photon 10 (1) (2018) 111–179.
[52] J. Wu, J. Li, R.K. Chan, A light sheet based high throughput 3D-imaging flow cytometer for phytoplankton analysis, Opt Express 21 (12) (2013) 14474–14480.
[53] M. Lin, Q. Liu, C. Liu, X. Qiao, C. Shao, X. Su, Label-free light-sheet microfluidic cytometry for the automatic identification of senescent cells, Biomed. Opt Express 9 (4) (2018) 1692–1703.
[54] R. Regmi, K. Mohan, P.P. Mondal, Light sheet based imaging flow cytometry on a microfluidic platform, Microsc. Res. Tech. 76 (11) (2013) 1101–1107.
[55] H. Jiang, T. Zhu, H. Zhang, J. Nie, Z. Guan, C.-M. Ho, et al., Droplet-based light-sheet fluorescence microscopy for high-throughput sample preparation, 3-D imaging and quantitative analysis on a chip, Lab Chip 17 (13) (2017) 2193–2197.
[56] P. Paiè, F. Bragheri, A. Bassi, R. Osellame, Selective plane illumination microscopy on a chip, Lab Chip 16 (9) (2016) 1556–1560.
[57] H. Shirahama, B.H. Lee, L.P. Tan, N.-J. Cho, Precise tuning of facile one-pot gelatin methacryloyl (GelMA) synthesis, Sci. Rep. 6 (1) (2016) 31036.
[58] J. Schindelin, I. Arganda-Carreras, E. Frise, V. Kaynig, M. Longair, T. Pietzsch, et al., Fiji: an open-source platform for biological-image analysis, Nat. Methods 9 (7) (2012) 676–682.
[59] P.J. Keller, A.D. Schmidt, J. Wittbrodt, E.H. Stelzer, Digital scanned laser light-sheet fluorescence microscopy (DSLM) of zebrafish and Drosophila embryonic development, Cold Spring Harb. Protoc. 2011 (10) (2011) prot065839.
[60] S. Berg, D. Kutra, T. Kroeger, C.N. Straehle, B.X. Kausler, C. Haubold, et al., ilastik: interactive machine learning for (bio) image analysis, Nat. Methods (2019) 1–7.
[61] J.-Y. Tinevez, N. Perry, J. Schindelin, G.M. Hoopes, G.D. Reynolds, E. Laplantine, et al., TrackMate: an open and extensible platform for single-particle tracking, Methods 115 (2017) 80–90.
[62] F.A. Holland, R. Bragg, 3 - flow of incompressible non-Newtonian fluids in pipes, in: F.A. Holland, R. Bragg (Eds.), Fluid Flow for Chemical Engineers, second ed., Butterworth-Heinemann, Oxford, 1995, pp. 96–139.
[63] R. Suntornnond, E.Y.S. Tan, J. An, C.K. Chua, A mathematical model on the resolution of extrusion bioprinting for the development of new bioinks, Materials 9 (9) (2016) 756.
[64] M.-A. Fardin, T. Ober, C. Gay, G. Grégoire, G. McKinley, S. Lerouge, Potential "ways of thinking" about the shear-banding phenomenon, Soft Matter 8 (4) (2012) 910–922.
[65] S. Granick, Soft matter in a tight spot, Phys. Today 52 (7) (1999) 26–31.
[66] S. Granick, Y. Zhu, H. Lee, Slippery questions about complex fluids flowing past solids, Nat. Mater. 2 (4) (2003) 221–227.
[67] A.-L. Vayssade, Flows of Herschel-Bulkley Fluids in Confined Environments: Applications to the Cementing of Oil Wells, 2015.
[68] J.F. Ortega-Avila, J. Pérez-González, B.M. Marín-Santibáñez, F. Rodríguez-González, S. Aktas, M. Malik, et al., Axial annular flow of a viscoplastic microgel with wall slip, J. Rheol. 60 (3) (2016) 503–515.
[69] S. Aktas, D.M. Kalyon, B.M. Marín-Santibáñez, J. Pérez-González, Shear viscosity and wall slip behavior of a viscoplastic hydrogel, J. Rheol. 58 (2) (2014) 513–535.
[70] B. Bhushan, J.N. Israelachvili, U. Landman, Nanotribology: friction, wear and lubrication at the atomic scale, Nature 374 (6523) (1995) 607–616.
[71] E.C. Achilleos, G. Georgiou, S.G. Hatzikiriakos, Role of processing aids in the extrusion of molten polymers, J. Vinyl Addit. Technol. 8 (1) (2002) 7–24.
[72] H. Lopez Hernandez, A.K. Grosskopf, L.M. Stapleton, G. Agmon, E.A. Appel, Non-Newtonian polymer–nanoparticle hydrogels enhance cell viability during injection, Macromol. Biosci. 19 (1) (2019), 1800275.
[73] L. Figueiredo, R. Pace, C. d'Arros, G. Réthoré, J. Guicheux, C. Le Visage, et al., Assessing glucose and oxygen diffusion in hydrogels for the rational design of 3D stem cell scaffolds in regenerative medicine, J. Tissue Eng. Regen. Med. 12 (5) (2018) 1238–1246.
[74] J. Yin, M. Yan, Y. Wang, J. Fu, H. Suo, 3D bioprinting of low-concentration cell-laden gelatin methacrylate (GelMA) bioinks with a two-step cross-linking strategy, ACS Appl. Mater. Interfaces 10 (8) (2018) 6849–6857.
[75] C.N. Holenstein, A. Horvath, B. Schär, A.D. Schoenenberger, M. Bollhalder, N. Goedecke, et al., The relationship between metastatic potential and in vitro mechanical properties of osteosarcoma cells, Mol. Biol. Cell 30 (7) (2019) 887–898.